Self-Assembly of the Ionic Liquid 1−Butyl−1−methylpyrrolidinium Bis-(trifluoromethylsulfonyl)imide on Graphite(0001): A Combined Experimental and Theoretical Investigation

Florian Buchner,[‡,a] *Katrin Forster-Tonigold,*[‡,a] *Maral Bozorgchenani,*[b] *Axel Gross,*[a,c] *and R. Jürgen Behm**[a,b]

[a] Helmholtz Institute Ulm, Electrochemical Energy Storage, Helmholtzstraße 11, D−89081 Ulm, Germany

[b] Ulm University, Institute of Surface Chemistry and Catalysis, Albert-Einstein-Allee 47, D−89081 Ulm, Germany

[c] Ulm University, Institute of Theoretical Chemistry, Albert-Einstein-Allee 11, D-89081 Ulm, Germany

Prof. Dr. R. J. Behm
Universität Ulm
Institut für Oberflächenchemie und Katalyse
Albert−Einstein−Allee 47
D−89069 Ulm, Germany
Phone: +49 (0)731/50−25451
Fax: +49 (0)731/50−25452

[‡] These authors contributed equally

E−Mail: juergen.behm@uni−ulm.de

ABSTRACT

The interaction between (sub-)monolayers of the ionic liquid (IL) 1-butyl-1-methyl-pyrrolidinium bis(trifluoromethylsulfonyl)imide $[BMP]^+[TFSA]^-$ and graphite(0001), which serves as a model for the anode|electolyte interface in Li-ion batteries, was investigated under ultrahigh vacuum (UHV) conditions, in a combined experimental and theoretical approach, employing high-resolution scanning tunneling microscopy (STM), X-ray photoelectron spectroscopy (XPS) and dispersion corrected density functional theory calculations (DFT-D). Importantly, we verified a balanced cation:anion ratio by XPS at 300 K and upon cool-down to ~100 K the coexistence of a mobile (2D) liquid and an ordered (2D) crystalline phase by STM. DFT-D calculations reveal $[BMP]^+$ and $[TFSA]^-$ stringed alternately in a row-like adsorption structure (cation−anion−cation−anion) that can be rationalized by electrostatic interactions between the ions. Simulated STM images of that structure closely resemble the experimental molecular resolved STM images and show that the features mostly stem from the cation.

TOC GRAPHICS

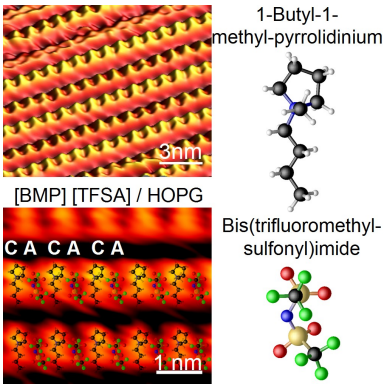

KEYWORDS: Ionic liquids, Li-ion batteries, electrode|electrolyte interface, scanning tunneling microscopy, dispersion corrected density functional theory, surface chemistry

Rechargeable lithium ion (Li-ion) batteries are state-of-the-art electrochemical energy storage devices that power a variety of portable electronic applications and electrical vehicles, but they are also promising candidates for highly efficient energy storage systems that compensate the volatile nature of renewable energy sources, like wind and solar energy. [1,2,3] Our motivation of the present study is the application of ionic liquids (ILs) as solvents in battery electrolyte, for improved performance and safety of next-generation Li-ion and Li-air batteries [4-6], whereat we deliberately concentrate on battery relevant 1-butyl-1-methyl-pyrrolidinium bis(trifluoromethylsulfonyl)imide ($[BMP]^+[TFSA]^-$). In general, ILs (molten organic salts with a melting point below 100°C per definition) present an intriguing class of components that received more and more attention in science and technology, [7-10] which is traced back to their versatile physicochemical properties that can be widely varied and thus adapted to specific applications by exploiting the almost unlimited possible anion/cation combinations. For example, their high ionic conductivity, electrochemical stability and low flammability are ideal for the use as solvents in electrolyte. According to this, numerous studies on the interaction between ILs and solid surfaces have been previously conducted, either *in situ* (electrochemical environment), [11-16] or *ex situ* (*in vacuo*). [17–22] Yet a drawback for the reliable use of Li-ion batteries is their limited energy density, irreversible capacity loss after charge/discharge cycles, and safety. [23] Thereby one of the most crucial aspects is a reaction that occurs at the electrode|electrolyte interface, as described, for example, by Arrora et al. for graphite electrodes, [24] which are in particular used as state-of-the-art ion-intercalation anodes. [25] In a Li-ion battery multiple components of the electrolyte (organic

solvents (ILs and / or carbonates) and a lithium (Li) salt (e.g. $LiPF_6$, $[Li]^+[TFSA]^-$) participate in this reaction and the consequent formation and characteristics of a passivating thin film known as solid|electrolyte interphase (SEI), which is built-up during the first potential cycles of battery operation, constituting a decisive role for the function and performance. [26] Despite of numerous investigations of these films (thickness of several nm up to µm), for example, by *post mortem* XPS, [26, 27] the SEI is still insufficiently understood and there is little information on the formation and composition of the SEI at the molecular scale. Thus, it is urgently required to explore the processes at the electrode|electrolyte interface at the molecular level. Thereby, the ordering of the molecules on the surface, the interactions between the molecules and with the surface, their intramolecular conformation and their chemical state are of particular interest, which is part of our ongoing model studies, in which we investigate the adsorption behavior of individual components of electrolytes like ILs [28-32] and carbonates [33] on well-defined flat model electrode surfaces under clean UHV conditions. While (sub-)monolayers of ILs have been investigated on noble and transition metal surfaces [28-32,34] and, one step further, to mimic electrolyte, the interactions between different electrolyte components, like IL+Li on Cu(111) [35] in the past, in this communication we report on the adsorption and structure formation of $[BMP]^+[TFSA]^-$ on graphite, which is a more frequently used anode material.

In general, *ex situ* microscopy investigations on the interaction of IL (sub-)monolayers on graphite(0001) in UHV are hardly available. For instance, Carstens et al. studied 1-methyl-3-octylimidazolium bis(trifluoromethylsulfonyl)imide ($[OMIM]^+[TFSA]^-$) on graphite by STM under UHV conditions at 100 K, however, they could not resolve molecules at the given conditions. [36] In contrast, by *in situ* STM measurement in $[OMIM]^+[TFSA]^-$ on graphite(0001) they acquired slightly differently ordered arrangements at cathodic potentials

of ~ - 2 V and correlated these to adsorbed cations, presumably with the octyl chains aligned along the graphite atomic lattice, but they conceded that the structure could maybe also be a bilayer. [36] Very recently, Elbourne et al. studied 1-ethyl-3-methylimidazolium bis(trifluoromethylsulfonyl)imide ($[EMIM]^+[TFSA]^-$) on graphite(0001) by *in situ* AFM and resolved a height-modulated row-like structure at open circuit potential. [37] Based on the changing dimension of the respective rows upon applying different potentials (± 0.3 V) they estimate that the adlayer could maybe be composed by an alternating sequence of anion−cation−cation−anion. However, all these *in situ* experiments did not rely on an unambiguous identification based on the distinct appearance of the molecules in STM. In our previous UHV study, anions and cations could unambiguously be identified at the $[BMP]^+[TFSA]^-$|Ag and Au interface by high resolution STM imaging under potential-free conditions. [28-30, 32] The combination of UHV STM and dispersion corrected Density Functional Theory (DFT-D) calculations demonstrated that the alkyl chain of the cation is pointing toward the vacuum and the anion is adsorbed in a *cis*-conformation with the oxygen atoms on the surface and the trifluoromethyl groups toward the vacuum next to the cation. [28] A similar identification of the molecules and details on the nature of the interaction at the IL|electrode interface would be the ultimate goal also on more battery-relevant graphite electrodes.

Herein we report results of a combined experimental and theoretical work on the adsorption behaviour of (sub-)monolayers of $[BMP]^+[TFSA]^-$ on a graphite(0001) model electrode under ultrahigh vacuum (UHV) conditions, employing scanning tunneling microscopy (STM), X-ray photoelectron spectroscopy (XPS) and dispersion corrected density functional theory (DFT-D) calculations. To the best of our knowledge, this is the first time that ions could be unambiguously identified at the IL|graphite interface and details on the interaction mechanism could be resolved, which is essentially needed for the detailed understanding of the processes

at the electrode|electrolyte interface. Finally, we believe that model studies like this are a promising route and essentially needed for the systematic improvement of future batteries.

A (sub-)monolayer of $[BMP]^+[TFSA]^-$ was vapor deposited on graphite(0001) at room temperature and the chemical state of the molecules was probed by XPS (Figure 1a,b; spectra at the bottom of each panel). For a better visibility of the peaks, the more intense multilayer spectra, which were acquired under the same conditions, were inserted as a reference (Figure 1a,b; spectra at the top of each panel). All spectra were acquired in the surface sensitive grazing emission mode (80° to the surface normal, information depth ~ 1 - 2 nm). For $[BMP]^+[TFSA]^-$ (sub-)monolayers in the C 1s spectral range the $C_{graphite}$ substrate peak is the dominating signal (284.4 eV) (Figure 1a). The C_{alkyl} peak (284.7 eV) (carbon atoms of the cation, which exhibit only carbon neighbors) is hidden below the substrate peak, $C_{hetereo}$ (286.7 eV) (carbon atoms of the pyrrolidium ring with a nitrogen neighbor) appears as a shoulder of $C_{graphite}$ at the high BE side and C_{anion} (carbon atoms of the anion with fluorine neighbors) is located at 292.8 eV. A reasonable fit was achieved by setting the peak area ratio to 5:4:2, which is the nominal ratio of C_{alkyl}:$C_{hetereo}$:C_{anion} in $[BMP]^+[TFSA]^-$. [27, 28] In addition, a shake up satellite of the main peak $C_{graphite}$ appears at around 290.5 eV. The N 1s signature of asdeposited $[BMP]^+[TFSA]^-$ (sub-)monolayers displays two contributions, which are assigned to the one nitrogen atom of the cation in the pyrrolidinium ring (N_{cation}) at 402.7 eV and to that of the anion (N_{anion}) at 399.5 eV, respectively (Figure 1b). The N_{cation} : N_{anion} intensity ratio of one, in conjunction with the peaks in the C 1s spectral range verify that $[BMP]^+[TFSA]^-$ is molecularly adsorbed on graphite(0001) at room temperature with a balanced cation:anion ratio. In addition, we found that the XP signals completely disappear upon heating to 450 – 500 K (Supporting Information (SI I)), *i.e.*, the molecules desorb without decomposition, which is similar to as $[BMP]^+[TFSA]^-$ on Ag(111) and Au(111), but different to as on

Cu(111), where the XPS measurements revealed a decomposition of the IL already slighty above room temperature to decomposition products like $CF_{x,ad}$, $SO_{x,ad}$, S_{ad}. [30]

Next, the $[BMP]^+[TFSA]^-$ (sub-)monolayer was cooled down to ~100 K. The STM image in Figure 2a displays the boundary between a highly ordered (2D) crystalline phase in which the molecular building blocks are arranged in row-like structures and an adjacent (2D) liquid/gas phase in which we see typically frizzy features, which are induced by rapidly diffusing species that are too mobile to be resolved by the scanning STM tip. Such a scenario is typical for a (2D) adsorption-desorption equilibrium between the two phases even at 100 K, which was also reported for $[BMP]^+[TFSA]^-$ on Ag(111). [28] To minimize tip induced effects we applied very mild tunneling conditions (U_t ~ −0.6 - −1.4 V, I_t ~ 10 - 20 pA, R_t ~ 30 - 140 GΩ), nevertheless, we found massive changes of the phase boundaries from image to image; often the entire (2D) crystalline phase disappeared; tip-induced effects could also play a role. The contour of the phase boundaries in Figure 2a,b is mostly straight in parallel to the rows and volatile perpendicular to them, which is indicative for stronger intra-row than inter-row interactions. This is already very different to the relatively straight and frizzy phase boundaries on Ag(111) [28] and a hint toward quite different interactions in the adlayer. In general, the observations at 100 K point toward (weakly) attractive intermolecular interactions and a low barrier for surface diffusion.

The high resolution STM images in Figure 2b,c highlight the (2D) crystalline phase. In Figure 2b a long-range ordered (2D) crystalline phase (30 × 30) nm^2 is homogeneously filling up the terrace with the molecular rows exhibiting inter-row distances of 1.55 ± 0.15 nm in average (the unusual high fluctuation of the inter-row distances is highlighted by the STM image in the Supporting Information SI II). Upon closer inspection of the images (Figure 2b,c), the assembly appears as an alternative sequence of rows with slightly different apparent

heights (Δh ~ 0.8 Å). The molecular features in each of the rows are elliptical protrusions with largely the same azimuthal orientation, exhibiting intra-row distances of 0.80 ± 0.03 nm. This is depicted by superimposed filled ellipsis (white), representative for the elevated rows and by unfilled ellipsis, representative for rows with decreased apparent height. We note that the images also reveal few rows, which are built-up by elliptical protrusions with a different azimuthal angle (marked with yellow ellipsis). We assume that the rather small height difference of the features is related to electronic effects, most likely arising from different adsorption sites. Interestingly, in contrast to the results on Ag(111) and Au(111) we did not observe pronounced circular protrusions, with an increased apparent height, which in combination with theory were assigned to the alkyl chains of the cations pointing toward the vacuum.

This indicates already a different adsorption geometry of the cation on graphite compared to the metal surfaces. We recently demonstrated that in the most stable configuration of an isolated $[BMP]^+$ cation the pyrrolidinium ring adopts an envelope conformation in which the butyl group either occupies the axial position (perpendicular to the ring) or the equatorial position (parallel to the ring). The equatorial position is energetically slightly more favorable (by 18 meV) for the isolated cation. [28] Hence, we assume that the cations could also adopt a conformation with the alkyl chain parallel to the ring on graphite(0001). The orientation of the alkyl chain with respect to the pyrrolidinium ring would also have a strong impact on the dimension of the molecular pattern on the surface. Indeed, the relatively large distance of 1.55 ± 0.15 nm between the molecular rows would allow that the cation adsorbs flat on graphite with the alkyl chain in equatorial position.

Based on this assumption about the cation´s configuration and the lattice parameters deduced from experimental STM images ($d_{inter\text{-}row}$ = 1.55 ± 0.15 nm, $d_{intra\text{-}row}$ = 0.80 ± 0.03 nm),

dispersion corrected DFT calculations lead to an adsorption structure in which $[BMP]^+$ and $[TFSA]^-$ are stringed alternately in a row (Figure 3a,b). $[TFSA]^-$ adopts a *cis*-orientation with respect to the S-N-S plane and the oxygen atoms point towards the surface. The nitrogen atom of $[TFSA]^-$ is about 5.59 Å above the graphite surface, whereas $[BMP]^+$ is much closer to the surface (distance N-graphite: 4.10 Å). Different configurations or conformations of the ions did not yield more stable adsorption structures: *e.g.*, an adsorption structure similar to the one shown in Figure 2a,b but with the *trans*-conformation of $[TFSA]^-$ is about 40 meV less stable, an adsorption structure in which the ions are fourfold coordinated by counterions is about 440 meV less stable. Furthermore, it is energetically most favorable when the alkyl chain of $[BMP]^+$ is aligned along the zig-zag axes of graphite(0001) (see Figure 3a), the molecular rows would concomitantly follow the armchair axes. However, other orientations of the alkyl chain are negligibly unfavorable by only 15 meV, which might tentatively explain the occurrence of few molecular rows with deviating azimuthal angles (see Figure 2b). A specific orientation of the domains is supported by STM images, which reveal different azimuthal orientation by multiplies of 120° (Supporting Information (SI III)), reflecting the symmetry of graphite(0001). Hence, these domains are rotationally aligned with respect to the graphite atomic lattice.

The relative orientation of $[BMP]^+$ and $[TFSA]^-$ in its most stable adsorption geometry can be rationalized when looking at the electrostatic potential mapped onto an isosurface of the charge density of the isolated ions (Figure 4). Such an analysis should provide an indication of the location of reactivity sites of a molecule with respect to the attack or attachment of charged particles, *i.e.*, whenever electrostatic interactions are decisive. Regions of the most positive electrostatic potential show where a negative charge prefers to attack, regions of the most negative electrostatic potential show where a positive charge prefers to attack. The

regions of $[TFSA]^-$ where a positive (partial) charge attaches preferentially (marked in red in Figure 3) are within the S-N-S plane both in front of and behind the N atom. The region of $[BMP]^+$ where a negative (partial) charge attaches preferentially (marked in blue in Figure 4) is located along the line defined by the N atom and the centre of the triangle formed by the three C atoms surrounding the N atoms. An arrangement of $[BMP]^+$ and $[TFSA]^-$ in the way that the regions of preferred attachment of the counterions of $[BMP]^+$ and $[TFSA]^-$ contact each other leads to a structure that is very similar to the most stable adsorption geometry of $[BMP]^+[TFSA]^-$ on graphite(0001).

Finally, the most stable adsorption structure is used to simulate STM images (Figure 3c,d). There is a fairly good agreement between the simulated STM image (Figure 2d) and the experimental STM images (Figures 2e,f). The protrusions observed in the STM image stem mostly from the cation with only slight contributions from the anion. In detail, the brightest spots are located at the positions of atoms of $[BMP]^+$ that are directly above C atoms of the uppermost graphene layer.

The adsorption energy of $[BMP]^+[TFSA]^-$ in its most stable adsorption structure on graphite(0001) is −1.51 eV. Adsorption in this structure is only possible due to dispersion interactions; the interaction energy based on pure RPBE values is repulsive by about 0.1 eV. Thus, dispersive forces play a decisive role in this system.

A detailed analysis of the interactions in the systems shows, that about half of the total adsorption energy is due to dispersion interaction between the ionic liquid and graphite ($E_{int(graphite\text{-}structure)} = -0.77$ eV, of which −1.31 eV are dispersion and 0.55 eV interactions calculated by pure RPBE). The other half of the adsorption energy is due to the interaction energy of the ion pairs within the structure ($E_{int(structure)} = -0.74$ eV, 40% dispersion and 60%

electrostatic interactions). Moreover, the interaction of ionic liquid pairs within the rows of the structure is about −0.73 eV whereas it is only about −5 meV perpendicular to the rows.

In conclusion, aiming toward a more detailed understanding of the molecular processes at model electrode surfaces during the formation of the electrode|electrolyte interphase we have investigated the interaction of (sub-)monolayers of the ionic liquid $[BMP]^+[TFSA]^-$ on a graphite(0001) model electrode and arrive at the following results and conclusions:

(1) From the XPS measurements of $[BMP]^+[TFSA]^-$ (sub-)monolayers we derived molecular adsorbed anions and cations with a balanced ratio at 300 K. After heating to 450 - 500 K the IL desorbs without decomposition.

(2) After vapor deposition of (sub-)monolayers of $[BMP]^+[TFSA]^-$ on graphite(0001) at room temperature and subsequent cool-down to around 100 K, the STM images show the coexistence of an ordered (2D) crystalline phase and a (2D) liquid phase. The fact that the STM images reveal an adsorption-desorption equilibrium between the two phases at ~100 K points to (weakly) attractive adsorbate-adsorbate interactions and a low surface diffusion barrier.

(3) The interactions between the ions in the (2D) crystalline phase are dominated by electrostatic ones. The specific charge distribution within the individual ions prompts $[BMP]^+$ and $[TFSA]^-$ to be stringed alternately in rows (cation−anion−cation−anion) when they are adsorbed on graphite(0001), whereby $[TFSA]^-$ is located farther from the surface. There is hardly any electronic interaction between $[TFSA]^-$ and the graphite(0001) surface. It is mainly the cation that leads to the observed elliptical protrusions in STM images. The alkyl chains of $[BMP]^+$ are preferentially aligned along the zig-zag axes of graphite(0001).

(4) About half of the adsorption energy is due to the electrostatic and dispersion interactions between the ions in the row. The remaining energy gain due to adsorption mainly stems from dispersion interactions between the graphite surface and the ionic liquid.

Overall, the study gained new and detailed insight into the interaction of $[BMP]^+[TFSA]^-$ (sub-)monolayers on graphite in a combined experimental and theoretical investigation. In the ongoing work, we envisage the coadsorption of two components of electrolyte, e.g., IL + Li.

Methods

Experimental Methods

The experiments were carried out in a commercial UHV system (SPECS) with a base pressure of 2×10^{-10} mbar. It consists of two chambers, one containing an Aarhus-type STM/AFM system (SPECS Aarhus SPM150 with Colibri sensor), which is capable of measurements in a temperature range of 90 and 370 K by cooling with LN_2 and resistive heating; the other one is equipped with an X-ray source (SPECS XR50, Al-K_α and Mg-K_α) and a hemispherical analyzer (SPECS, DLSEGD-Phoibos-Has3500) for XPS measurements.

The highly oriented pyrolytical graphite(0001) (HOPG) single crystal was purchased from MaTeck (ZYA, mosaic spread 0.4°±0.1°). Samples used for the XPS measurements exhibited a cuboid shape with a size of $10 \times 10 \times < 1$ mm and for STM measurements of $5 \times 5 \times < 0.6$ mm, respectively. The HOPG was freshly cleaved, fixed on a tantalum sample plate with silver conductive paste, transferred into the load lock and subsequently into the UHV chamber, where the sample was first annealed at 900 K for 2 h to generate a clean graphite(0001) substrate.

The ionic liquid was filled into a quartz crucible, which was mounted in a Knudsen effusion cell (Ventiotec, OVD−3). The IL was then degassed for at least 24 h under UHV conditions at room temperature, followed by several hours of degassing at up to 400 K. The cleanness of the IL vapor was tested with a quadrupole mass spectrometer (Pfeiffer HiQuad QMA 400). To generate IL adlayers on graphite(0001), we evaporated the IL at a temperature of the IL source of 450 K. Under these conditions the deposition rate was ~ 0.1 ML min^{-1}.

STM measurements were performed in constant current mode with currents between 10 and 20 pA and bias voltages between -0.6 and -1.4 V (applied to the sample).

For XPS measurements we used an Al-K_α X-ray source (1486.6 eV), operated at a power of 250 W (U = 14 kV, I = 17.8 mA). The spectra were recorded at pass energy of 100 eV at grazing emission (80° to the surface normal). For the fitting of the XP spectra a simultaneous fit of background (Shirley + slope) and signal was used, applying an asymmetric pseudo-Voigt-type function. [38]

Calculational Methods

Periodic DFT-calculations were performed using the revised version of the exchange-correlation functional of Perdew, Burke and Ernerhof (RPBE) [39] as implemented in the Vienna *ab initio* simulation package (VASP). [40,41] In order to account for dispersive interactions missing in the exchange-correlation functionals of the generalized gradient approximation (GGA), we employed Grimme's correction scheme of 2010 (DFT-D3) in connection with a damping function proposed by Chai and Head-Gordon (“zero-damping”). [42,43] It has recently been shown that this approach yields reliable adsorption energies and structures for organic molecules and hydrogen-bonded networks on metal surfaces. [44-46] In particular using dispersion corrected RPBE methods instead of dispersion corrected PBE

methods improved the description of systems where electrostatic interactions and dispersion interactions are crucial. [45,47] Ion cores are represented by means of the projector augmented wave (PAW) method. [48,49] The electronic one-particle wave functions were expanded in a plane wave basis set up to an energy cut-off of 400 eV.

The graphite(0001) surface was represented by a slab consisting of 3 graphene layers, separated by a vacuum region of about 23 Å. According to the lattice parameters of the overlayer structure determined from the experimental STM images rectangular unit cells with the dimensions (8.581×14.863) Å^2 for calculations employing RPBE-D3 and (8.544×14.799) Å^2 for calculations employing PBE-D3 have been chosen. For the integration over the first Brillouin zone a $5 \times 3 \times 1$ Monkhorst-Pack k-point mesh [50] with a Gaussian smearing of 0.05 eV was employed. The geometry of the adsorption complex was optimized by relaxing all atoms of the IL pair and the atoms of the uppermost graphene layer. The adsorption energy (E_{ad}) calculates as $E_{ad} = E_{(\text{adsorption structure})} - E_{([BMP][TFSA])}$, whereby $E_{(\text{adsorption structure})}$ denotes the energy of the optimized adsorption complex and $E_{([BMP][TFSA])}$ is the energy of an optimized $[BMP]^+[TFSA]^-$ pair within a large box.

Although there is no unambiguous way to portion the adsorption energy, its contributions from adsorbate-adsorbate and graphite-adsorbate interactions, it can give some hints into the relative importance of the interactions occurring in the system. We calculated the interaction energy between the adsorption structure and an optimized free standing layer of the ionic liquid with the same unit cell ($E_{(layer)}$) $E_{int(\text{graphite-structure})} = E_{(\text{adsorption structure})} - E_{(layer)}$, as well as the interaction energy between this free standing layer of the ionic layer and an isolated $[BMP]^+$ $[TFSA]^-$ pair $E_{int(structure)} = E_{(layer)} - E_{([BMP][TFSA])}$.

All adsorption and interaction energies are given with respect to one $[BMP]^+[TFSA]^-$ pair.

STM simulations are based on the Tersoff-Hamann approximation. [51] Within that model the tunneling current is proportional to the local density of states (LDOS) at the surface close to the Fermi energy at the position of the tip. Constant-current images are simulated by an isosurface of the LDOS integrated between the Fermi energy of the system and the sample bias.

Isolated ions have also been calculated using the PBE functional as implemented in the GAUSSIAN09 code [52] in connection with the atom centered basis set aug-cc-pVTZ. [53-55] For isolated molecules no dispersion corrections have been employed.

Figures

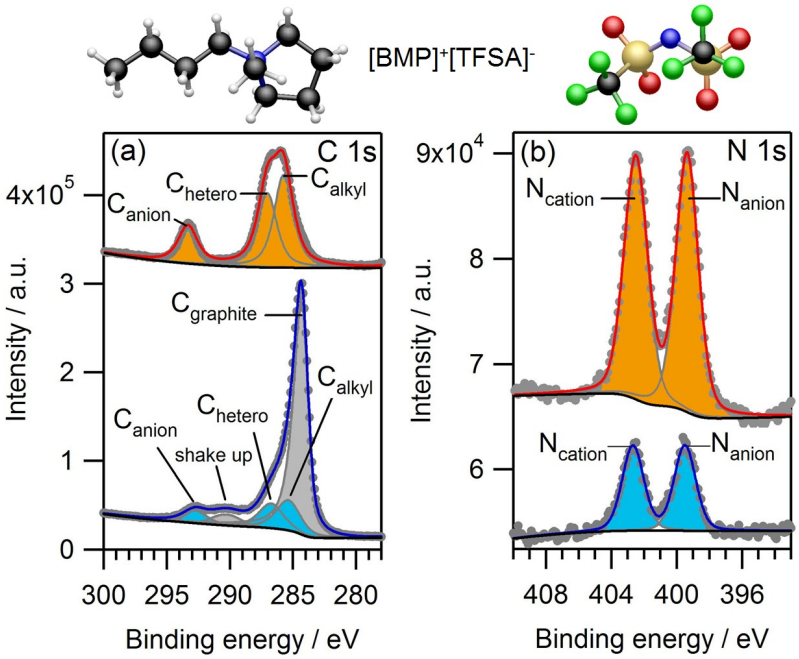

Figure 1. (a) and (b) XP C 1s and N 1s spectra of (sub-)monolayers of $[BMP]^+[TFSA]^-$ on a graphite(0001) recorded at r.t. (bottom of each panel); multilayer reference spectra are shown on top of each panel. A molecular representation of $[BMP]^+[TFSA]^-$ is inserted above the panels. Atoms are color coded C (black), N (blue), O (red), S (gold), and F (green).

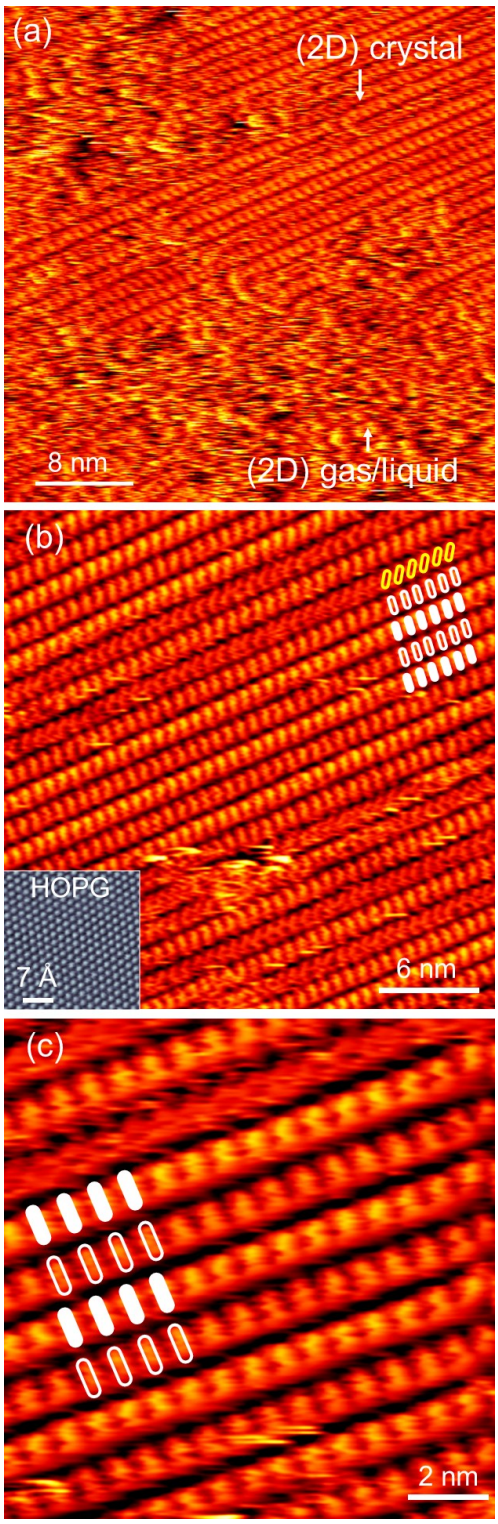

Figure 2. (a) STM image of (sub-)monolayers of $[BMP]^+[TFSA]^-$ on graphite(0001) after vapour deposition on the substrate held at r.t and subsequent cool down to ~100 K ((a) U = −1.40 V, I = 10 pA; (b) U = −1.00 V, I = 20 pA; (c) U = −0.78 V, I = 20 pA).

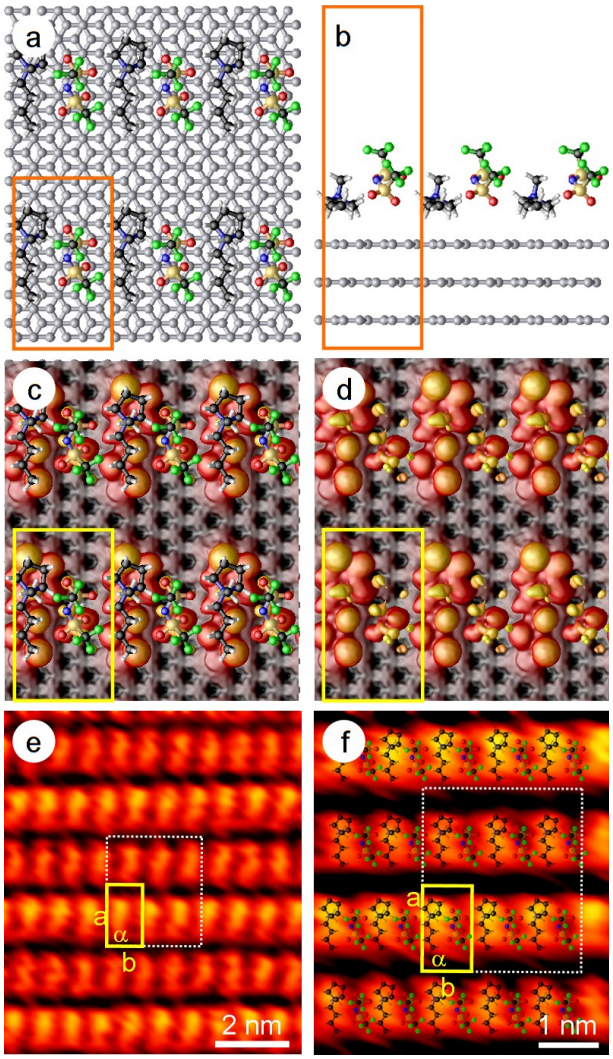

Figure 3. (a,b) Top and side view, respectively, of the most stable adsorption structure of $[BMP]^+[TFSA]^-$ on graphite(0001). (c,d) Simulated STM images of the structure shown in (a,b). (U = −0.78 eV, isosurface value = 5E−7 e/Å3) (e,f) Experimental STM image for comparison; the lattice constants are: a = 1.55 ± 0.15 nm, b = 0.80 ± 0.03 nm, α ~ 90° ((e) U = −1.00 V, I = 20 pA; U = −0.78 V, I = 20 pA).

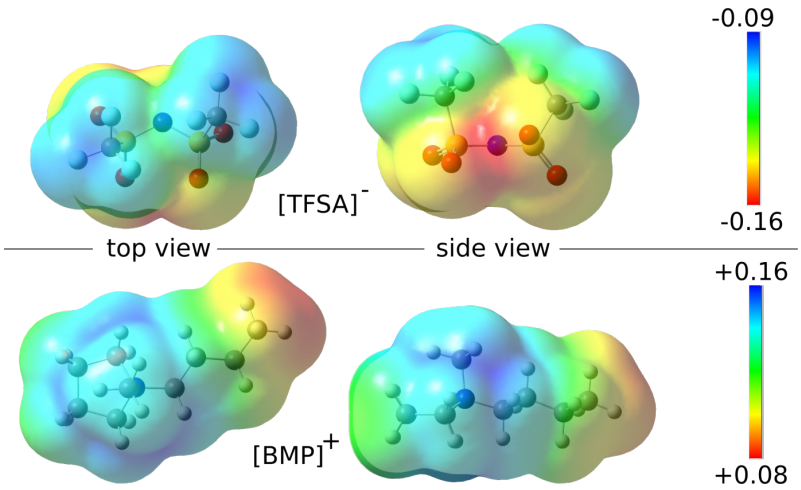

Figure 4. Electrostatic potential (in hartree/e) mapped onto an isosurface (isosurface value = 4E−4 e/a03) of the total charge density of $[TFSA]^-$ (upper figures) and $[BMP]^+$ (lower figures). The blue regions reveal the most positive electrostatic potential a positive test charge experiences, *i.e.*, they show regions where a negative charge would attack preferentially. In contrast the red regions reveal the most negative electrostatic potential a positive test charge experiences, *i.e.*, they show regions where a positive charge would attack preferentially.

ASSOCIATED CONTENT

Supporting Information. XP spectra of asdeposited $[BMP]^+[TFSA]^-$ (sub-)monolayers on graphite(0001) at room temperature and after anealing to 450 - 500 K. STM images of $[BMP]^+[TFSA]^-$ (sub-)monolayers at around 100 K. This material is available free of charge via the Internet at http://pubs.acs.org.

AUTHOR INFORMATION

Corresponding Author

*Phone: +49 (0)731/50-25451. Fax: +49 (0)731/50-25452.

Email: juergen.behm@uni−ulm.de

Notes

The authors declare no competing financial interests.

ACKNOWLEDGMENT

This work was supported by the Bundesministerium für Bildung und Forschung in the project LiEcoSafe under contract number 03X4636C.

REFERENCES

1 Etacheri, V.; Marom, R.; Elazari, R.; Salitra; G.; Aurbach, D. Challenges in the Development of Advanced Li-ion Batteries: a Review. *Energy Environ. Sci.* **2011**, *4*, 3243-3262.

2 Scrosati, B.; Garche, J. Lithium Batteries: Status, Prospects and Future. *Journal of Power Sources*, 2010, **195**, 2419.

3. Erickson, E. M.; Ghanty, C.; Aurbach D. New Horizons for Conventional Lithium Ion Battery Technology. *J. Phys. Chem. Lett.*, **2014**, *5*, 3313−3324.

4. Armand, M.; Tarascon, J.-M. Building Better Batteries. *Nature* **2008,** *451*, 652−657.

5. Armand, M.; Endres, F.; MacFarlane, D. R.; Ohno, H.; Scrosati, B. Ionic−liquid Materials for the Electrochemical Challenges of the Future. *Nature Mater.* **2009,** *8*, 621−629.

6. Girishkumar, G.; McCloskey, B.; Luntz, A. C.; Swanson, S.; Wilcke, W. Lithium−Air Battery: Promise and Challenges. *J. Phys. Chem. Lett.* **2010,** *1*, 2193−2203.

7. Welton, T. Room-Temperature Ionic Liquids. Solvents for Synthesis and Catalysis. *Chem. Rev.* **1999,** *99*, 2071-2084.

8. Wasserscheid, P.; Keim, W. Ionic Liquids—New "Solutions" for Transition Metal Catalysis. *Angew. Chem. Int. Ed.* **2000,** *39*, 3772-3789.

9. Plechkova, N. V.; Seddon, K. R. Applications of Ionic Liquids in the Chemical Industry. *Chem. Soc. Rev.* **2008,** *37*, 123-150.

10. Smiglak, M.; Pringle, J. M.; Lu, X.; Han, L.; Zhang, S.; Gao, H.; MacFarlane, D. R.;Rogers, R. D. Ionic Liquids for Energy, Materials, and Medicine. *Chem. Commun. Chem.Commun*. **2014**, *50*, 9228-9250.

11. Atkin, R.; El Abedin, S. Z.; Hayes, R.; Gasparotto, L. H. S.; Borisenko, N.; Endres, F. AFM and STM Studies on the Surface Interaction of [BMP]TFSA and [EMIm]TFSA Ionic Liquids with Au(111). *J. Phys. Chem. C* **2009,** *113*, 13266−13272.

12. Endres, F.; Höfft, O.; Borisenko, N.; Gasparotto, L. H. S.; Prowald, A.; Al Salman, R.; Carstens, T.; Atkin, R.; Bund, A.; El Abedin, S. Z. Do Solvation Layers of Ionic Liquids Influence Electrochemical Reactions? *Phys. Chem. Chem. Phys.* **2010,** *12*, 1724−1732.

13. Drüschler, M.; Borisenko, N.; Wallauer, J.; Winter, C.; Huber, B.; Endres, F.; Roling, B. New Insights into the Interface between a Single−Crystalline Metal Electrode and an Extremely Pure Ionic Liquid: Slow Interfacial Processes and the Influence of Temperature on Interfacial Dynamics. *Phys. Chem. Chem. Phys.* **2012,** *14*, 5090−5099.

14. Gnahm, M.; Berger, C.; Arkhipova, M.; Kunkel, H.; Pajkossy, T.; Maas, G.; Kolb, D. M. The Interfaces of Au(111) and Au(100) in a Hexaalkyl−Substituted Guanidinium Ionic Liquid: an Electrochemical and *in Situ* STM Study. *Phys. Chem. Chem. Phys.* **2012,** *14*, 10647−10652.

15. Müller, C.; Vesztergom, S.; Pajkossy, T.; Jacob, T. The Interface between Au(100) and 1−butyl−3−methyl−imidazoliumbis(trifluoromethylsulfonyl)imide. *J. Electroanal. Chem.* **2015**, *737*, 218–225.

16. Wen, R., Rahn, B., Magnussen, O. M. Potential-Dependent Adlayer Structure and Dynamics at the Ionic Liquid / Au(111) Interface: A Molecular Scale In Situ STM Video/STM Study. *Angew. Chem. Int. Ed.*, **2015**, *54*, 6062 –6066.

17. Steinrück, H.-P.; Libuda, J.; Wasserscheid, P.; Cremer, T.; Kolbeck, C.; Laurin, M.; Maier, F.; Sobota, M.; Schulz, P. S.; Stark, M. Surface Science and Model Catalysis with Ionic Liquid−Modified Materials . *Adv. Mater.* **2011,** *23*, 2571−2587.

18. Steinrück, H.-P. Recent Developments in the Study of Ionic Liquid Interfaces Using X−ray Photoelectron Spectroscopy and Potential Future Directions. *Phys. Chem. Chem. Phys.* **2012,** *14*, 5010−5029.

19. Steinrück, H.-P.; Wasserscheid, P. Ionic Liquids in Catalysis. *Catal. Lett.* **2015**, *145*, 380–397.

20. Lovelock, K. R. J.; Villar−Garcia, I. J.; Maier, F.; Steinrück, H.-P.; Licence, P. Photoelectron Spectroscopy of Ionic Liquid−Based Interfaces. *Chem. Rev.* **2010,** *110*, 5158−5190.

21. Höfft, O.; Bahr, S.; Himmerlich, M.; Krischok, S.; Schaefer, J. A.; Kempter, V. Electronic Structure of the Surface of the Ionic Liquid [EMIM][Tf_2N] Studied by Metastable Impact Electron Spectroscopy (MIES), UPS, and XPS. *Langmuir* **2006,** *22*, 7120−7123.

22. Syres, K. L.; Jones, R. G. Adsorption, Desorption, and Reaction of 1-Octyl-3-methylimidazolium Tetrafluoroborate, [C8C1Im][BF4], Ionic Liquid Multilayers on Cu(111). *Langmuir*, **2015**, 31 (36), 9799–9808.

23. Tarascon, J.M.; Armand, M. Issues and Challenges Facing Rechargeable Lithium Batteries. *Nature*, **2001**, *414*, 359-367.

24. Arora, P., White, R.E., Doyle, M. Capacity Fade Mechanism and Side Reactions in Lithium-Ion Batteries. *J. Electrochem. Soc.,* **1998**, 3647-3667**.**

25. Persson, K.; Sethuraman, V. A.; Hardwick, L. J.; Hinuma, Y.; Meng, Y. S.; van der Ven, A.; Srinivasan, V.; Kostecki, R.; Ceder, G. Lithium Diffusion in Graphitic Carbon. *J. Phys. Chem. Lett.,* **2010**, *1*, 1176–1180.

26. Verma, P.; Maire, P.; Novak, P. A Review of the Features and Analyses of the Solid Electrolyte Interphase in Li−ion Batteries. *Electrochim. Acta* **2010**, *55*, 6332−6341.

27. Xu, C.; Sun, B.; Gustafsson, T.; Edström, K.M; Brandell, D.; Hahlin, M. Interface Layer Formation in Solid Polymer Electrolyte Lithium Batteries: an XPS Study. *J. Mater. Chem. A* **2014**, *2*, 7256−7264.

28. Buchner, F.; Forster−Tonigold, K.; Uhl, B.; Alwast, D.; Wagner, N.; Farkhondeh, H.; Groß, A.; Behm, R. J. Toward the Microscopic Identification of Anions and Cations at the Ionic Liquid|Ag(111) Interface: A Combined Experimental and Theoretical Investigation. *ACS Nano*, **2013**, *7*, 7773−7784.

29. Uhl, B.; Cremer, T.; Roos, M.; Maier, F.; Steinrück, H.-P.; Behm, R. J. At the Ionic Liquid|Metal Interface: Structure Formation and Temperature Dependent Behavior of an Ionic Liquid Adlayer on Au(111). *Phys. Chem. Chem. Phys.*, **2013**, *15*, 17295−17302.

30. Uhl, B.; Buchner, F.; Alwast, D.; Wagner, N.; Behm, R. J. Adsorption of the Ionic Liquid [BMP][TFSA] on Au(111) and Ag(111): Substrate Effects on the Structure Formation Investigated by STM. *Beilstein J. Nanotechnol.* **2013**, *4,* 903−918.

31. Uhl, B.; Buchner, F.; Gabler, S.; Bozorgchenani, M.; Behm, R. J. Adsorption and Reaction of Sub−monolayer Films of an Ionic Liquid on Cu(111). *Chem. Commun.* **2014**, *50*, 8601−8604.

32. Uhl, B.; Huang, H.; Alwast, D.; Buchner, F.; Behm, R. J. Interaction of Ionic Liquids with Noble Metal Surfaces: Structure Formation and Stability of [OMIM][TFSA] and [EMIM][TFSA] on Au(111) and Ag(111). *Phys. Chem. Chem. Phys.*, **2015**, *17*, 23816−23832.

33. Buchner, F.; Farkhondeh, H.; Bozorgchenani, M.; Uhl, B.; Behm, R. J. Temperature-induced Structural and Chemical Changes of Ultrathin Ethylene Carbonate Films on Cu(111). *Phys. Chem. Chem. Phys.* **2014**, *16*, 11191−11195.

34. Foulston, R.; Gangopadhyay, S.; Chiutu, C.; Moriarty, P.; Jones, R. G. Mono- and Multi-Layer Adsorption of an Ionic Liquid on Au(110). *Phys. Chem. Chem. Phys.* **2012,** *14*, 6054−6066.

35. Buchner F., Bozorgchenani, M., Uhl, B., Farkhondeh, H., Bansmann, J., Behm R. Reactive Interaction of (Sub-)monolayers and Multilayers of the Ionic Liquid 1-Butyl-1-methylpyrrolidinium Bis(trifluoro-methylsulfonyl)imide with Coadsorbed Lithium on Cu(111), *J. Phys. Chem. C*, **2015**, *119 (29)*, 16649–16659.

36. Carstens, T., Gustus, R., Höfft, O., Borisenko, N., Endres, F., Li, H., Wood, R. J., Page, A. J., Atkin, R. Combined STM, AFM, and DFT Study of the Highly Ordered Pyrolytic Graphite/1-Octyl-3-methyl-imidazolium Bis(trifluoromethylsulfonyl)imide Interface *J. Phys. Chem. C*, **2014**, *118*, 10833–10843.

37. Elbourne, A.; McDonald, S.; Voïchovsky, K; Endres, F.;Warr, G. G.; Atkin, R. Nanostructure of the Ionic Liquid–Graphite Stern Layer. *ACS Nano* **2015**, *9 (7)*, 7608–7620.

38. Schmid, M.; Steinrück, H.-P.; Gottfried, J.M. A New Asymmetric Pseudo-Voigt Function for More Efficient Fitting of XPS Lines. *Surf. Interface Anal.* **2014**, *46*, 505–511.

39. Hammer, B.; Hansen, L. B.; Nørskov, J. K. Improved Adsorption Energetics within Density-functional Theory using Revised Perdew-Burke-Ernzerhof Functionals. *Phys. Rev. B* **1999**, *59*, 7413−7421.

40. Kresse, G.; Furthmüller, J. Efficiency of *ab Initio* Total Energy Calculations for Metals and Semiconductors Using a Plane-Wave Basis Set. *J. Comp. Mat. Sci.* **1996,** *6*, 15−50.

41. Kresse, G.; Furthmüller, J. Efficient Iterative Schemes for *ab Initio* Total-Energy Calculations Using a Plane-Wave Basis Set . *Phys. Rev. B* **1996,** *54*, 11169−11186.

42. Grimme, S.; Antony, J.; Ehrlich, S.; Krieg, H. A Consistent and Accurate ab Initio Parametrization of Density Functional Dispersion Correction (DFT-D) for the 94 Elements H-Pu. *J. Chem. Phys.* **2010**,*132*, 154104−154119.

43. Chai, J.-D.; Head-Gordon M. Long-range Corrected Hybrid Density Functionals with Damped Atom–atom Dispersion Corrections. *Phys. Chem. Chem. Phys*. **2008**, *10*, 6615−6620.

44. Tonigold, K.; Groß, A. Adsorption of Small Aromatic Molecules on the (111) Surfaces of Noble Metals: A Density Functional Theory Study with Semiempirical Corrections for Dispersion Effects. *J. Chem. Phys.* **2010,** *132*, 224701−10.

45. Tonigold, K.; Groß, A. Dispersive Interactions in Water Bilayers at Metallic Surfaces: A Comparison of the PBE and RPBE Functional Including Semiempirical Dispersion Corrections. *J. Comput. Chem.* **2012,** *33*, 695−701.

46. Waldmann, T.; Nenon, C.; Tonigold, K.; Hoster, H. E.; Groß, A.; Behm, R. J. The Role of Surface Defects on Large Organic Molecule Adsorption: Substrate Configuration Effects. *Phys. Chem. Chem. Phys.* **2012,** *14*, 10726−10731.

47. Katrin Forster-Tonigold and Axel Groß, Dispersion corrected RPBE studies of liquid water, *J. Chem. Phys*. **2014**, *141*, 064501−5.

48. Blöchl, P. E. Projector Augmented-Wave Method. *Phys. Rev. B* **1994,** *50*, 17953−17979.

49. Kresse, G.; Joubert, D. From Ultrasoft Pseudopotentials to the Projector Augmented-Wave Method. *Phys. Rev. B* **1999,** *59*, 1758−1775.

50. Monkhorst, H. J.; Pack, J. D. Special Points for Brillouin-Zone Integrations. *Phys. Rev. B* **1976,** *13*, 5188−5192.

51. Tersoff, J.; Hamann, D. R. Theory of the Scanning Tunneling Microscope. *Phys. Rev. B* **1985**, *31*, 805−813.

52. Frisch, M. J.; Trucks, G. W.; Schlegel, H. B.; Scuseria, G. E.; Robb, M. A.; Cheeseman, J. R.; Scalmani, G.; Barone, V.; Mennucci, B.; Petersson, G. A.; *et al.* Gaussian 09, Revision B.01, Gaussian, Inc., Wallingford CT. Gaussian. **2010**.

53. Dunning Jr., T. H. Gaussian Basis Sets for Use in Correlated Molecular Calculations. I. The Atoms Boron through Neon and Hydrogen. *J. Chem. Phys.* **1989**, *90*, 1007−1023.

54. Kendall, R. A.; Dunning, J.; Harrison, R. J. Electron Affinities of the First-row Atoms Revisited. Systematic Basis Sets and Wave Functions. *J. Chem. Phys.* **1992,** *96*, 6796−6806.

55. Woon, D. E.; Dunning, J. Gaussian Basis Sets for Use in Correlated Molecular Calculations. III. The Atoms Aluminum through Argon. *J. Chem. Phys.* **1993,** *98*, 1358−1371.